

Scalar Casimir-Polder forces for uniaxial corrugations

Babette Döbrich^{1,2,3}, Maarten DeKieviet³, and Holger Gies^{1,2*}

¹ *Theoretisch-Physikalisches Institut, Friedrich-Schiller-Universität Jena*

Max-Wien-Platz 1, D-07743 Jena, Germany

² *Institut für Theoretische Physik, Universität Heidelberg*

Philosophenweg 16, D-69120 Heidelberg, Germany

³ *Physikalisches Institut, Universität Heidelberg*

Philosophenweg 12, D-69120 Heidelberg, Germany

Abstract

We investigate the Dirichlet-scalar equivalent of Casimir-Polder forces between an atom and a surface with arbitrary uniaxial corrugations. The complexity of the problem can be reduced to a one-dimensional Green's function equation along the corrugation which can be solved numerically. Our technique is fully nonperturbative in the height profile of the corrugation. We present explicit results for experimentally relevant sinusoidal and sawtooth corrugations. Parameterizing the deviations from the planar limit in terms of an anomalous dimension which measures the power-law deviation from the planar case, we observe up to order-one anomalous dimensions at small and intermediate scales and a universal regime at larger distances. This large-distance universality can be understood from the fact that the relevant fluctuations average over corrugation structures smaller than the atom-wall distance.

1 Introduction

Casimir forces [1] between mesoscopic or macroscopic objects as well as Casimir-Polder forces [2] between an atom and a surface can be attributed to a reordering of fluctuations in the quantum vacuum. Recent years have witnessed considerable progress in measuring these forces [3, 4, 5, 6], paving the way for future application in micro- and nanomechanical engineering and single-atom manipulation.

Particularly for such applications, standard calculational techniques for simple flat surfaces are insufficient and a profound understanding of the influence of geometry on these

*E-mail: babette.doebrich@uni-jena.de, maarten.dekieviet@physik.uni-heidelberg.de, gies@tpi.uni-jena.de

quantum forces is required. In fact, since fluctuations occur on all momentum or length scales, quantum forces are strongly affected by the global properties of a given system. From a technical perspective, global properties such as geometry or curvature dependencies generally require a full understanding of the fluctuation spectrum in a given configuration and cannot be dealt with by perturbative expansions with respect to a small geometry parameter.

Therefore, a variety of new field-theoretical methods for understanding and computing fluctuation phenomena have been developed in the past few years, such that early phenomenological recipes, such as the proximity force approximation (PFA) [7] have been overcome by now. Apart from exact results in certain asymptotic limits [8, 9] and more controllable approximation techniques [10, 11], field-theoretical worldline methods have lead to efficient algorithms for Casimir energies [12, 13, 14]. In addition, approaches based on scattering theory have proved most successful for finding new exact solutions and efficient computation schemes [15, 16, 17, 18, 19, 20, 21, 22], see [23] for a recent review. New results with direct mode summation have been obtained in [24]; numerical tools based on brute-force discretization have been used in [25].

Many of these approaches can be directly linked with a constrained-functional-integral formulation, as first introduced in [26] for the parallel-plate case and further developed for corrugated surfaces in [27] and lastly extended to general dispersive forces between structured media [28]. For Casimir forces involving corrugated surfaces, results based on a perturbative expansion in the height profile have been obtained recently [29].

Whereas most of these approaches have been mainly applied to Casimir forces between extended objects, the Casimir-Polder force between an atom and a surface of general shape has not been so widely studied. An estimate of the influence of surface roughness has been given in [30], where an additivity approximation has been perturbatively expanded in the roughness amplitude. In [31], it was pointed out that large geometry corrections to the Casimir-Polder force should be observable for atoms in front of a corrugated surface, potentially visible in experiments with cold atoms near a surface. These studies were based on a perturbative analysis in the height profile. If the height-profile parameters are of the same order as the atom-wall distance, however, geometry plays a much more dominant role and perturbative theory is expected to be no longer appropriate. Whereas cold atom gas experiments become increasingly difficult in this regime, Casimir-Polder force measurements can be well controlled in this regime. In particular the atomic beam spin echo technique introduced in [32, 33, 5] has recently demonstrated high resolution access to some of the fundamental issues concerning Casimir interactions. Experimental results on geometrical effects will be presented elsewhere shortly [34].

This work is devoted to a nonperturbative study of Casimir-Polder forces near a surface with uniaxial corrugation. Our method is based on the constrained-functional-integral approach which facilitates to map the core part of the problem onto a one-dimensional Green's function problem along the direction of nontrivial curvature of the surface. As this Green's function problem involves singular kernels, we identify an appropriate representation which is accessible to stable and efficient numerical tools. For simplicity, we consider a fluctuating scalar field obeying Dirichlet boundary conditions instead of the full electromagnetic

field. Hence, our results should not be directly applied to realistic atom-wall studies; they are applicable to Casimir configurations in ultracold-gas systems as suggested in [35]. Our method is not restricted to Dirichlet scalars and can straightforwardly be generalized to the electromagnetic case.

The paper is organized as follows: In Sect. 2, we review the treatment of Casimir forces within scalar QFT and give the general Casimir energy for two Dirichlet surfaces. Within this formulation, we then evaluate the Casimir energy in Sect. 3 for a sphere and a planar surface in the limit $\frac{r}{H} \ll 1$ to first order explicitly. This limit defines the scalar analogue of the Casimir-Polder force. In Sect. 4, we extend our technique to the case of uniaxially corrugated surfaces. In Sect. 5, we present numerical results for the scalar Casimir-Polder potential for a sinusoidally shaped surface as well as for a saw tooth profile, both of which have been used in experiments [34]. Conclusions are given in Sect. 7.

2 Scalar field theory with boundaries

The Casimir energy of a system is given by the shift of the ground state energy caused by the presence of boundaries imposing constraints on the fluctuating field. For calculating Casimir forces between disconnected bodies, only the Casimir interaction energy is relevant. The latter corresponds to that part of the ground state shift which depends on the relative position and orientation of all bodies. The Casimir self-energies of single bodies are irrelevant for the Casimir force.

Here, we investigate the Casimir interaction energy induced by fluctuations of a scalar field ϕ . We follow the constrained-functional-integral approach [26], which is introduced in the following in a brief and simplified manner, see [26, 27, 39, 20] for a more detailed discussion and generalizations. We start from the associated Euclidean generating functional,

$$\mathcal{Z} = \int \mathcal{D}\phi \exp\left(-\frac{1}{2\hbar} \int d^4x (\partial\phi(x))^2\right). \quad (1)$$

The Casimir interaction energy of a system bounded by two surfaces, whose relative position is specified (e.g., by a (mean) separation H), is then given by

$$E(H) = -\frac{\hbar c}{T_E} \ln \frac{\mathcal{Z}_{\text{B.C.}}}{\mathcal{Z}_\infty}, \quad (2)$$

where $\mathcal{Z}_{\text{B.C.}}$ stands for the generating functional of the fluctuating field obeying the system's boundary conditions, whereas \mathcal{Z}_∞ represents the case of infinite separation between the objects, i.e., $H \rightarrow \infty$. In this way, irrelevant Casimir self-energies are subtracted. The length in Euclidean time direction is denoted by T_E .

The boundary conditions for the fields are implemented by insertion of a δ functional constraint into \mathcal{Z} . For the case of Dirichlet boundary conditions, the corresponding δ functional can be represented by product of δ functions $\delta(\phi(x_\alpha))$ for all 4-vectors x_α pointing onto a surface S_α ; here, α labels multiple disjoint surfaces. Hence, $\mathcal{Z}_{\text{B.C.}}$ for

Dirichlet boundaries in the case of two plates is given by

$$\mathcal{Z}_D = \int \mathcal{D}\phi \prod_{\alpha=1}^2 \prod_{x_\alpha} \delta(\phi(x_\alpha)) \exp\left(-\frac{1}{2\hbar} \int d^4x (\partial\phi(x))^2\right). \quad (3)$$

In order to evaluate the integral over the fields ϕ , a Fourier representation is used for the δ functional with the help of auxiliary fields that have support only on the surfaces S_α .¹ First performing the Gaussian integral over ϕ leaves us – apart from an irrelevant factor – with another Gaussian integral for the auxiliary fields which can also be carried out, yielding for the Casimir interaction energy,

$$E(H) = \frac{\hbar c}{T_E} \frac{1}{2} \text{Tr} \ln(\mathcal{M}_\infty^{-1} \mathcal{M}), \quad (4)$$

where \mathcal{M} denotes a matrix whose entries are the propagators of the fluctuating scalar, i.e., the Green's function of the Laplacian in this case,

$$\mathcal{M}_{\alpha\beta}(x, x') = \frac{1}{4\pi^2} \frac{1}{(x_\alpha - x'_\beta)^2}, \quad (5)$$

with four-vectors x and x' pointing onto the surfaces S_α and S_β , respectively. At the same time, \mathcal{M} is the inverse of the auxiliary-field propagator on the surfaces. Complications of Eq. (4) are hidden in the fact that the trace has to be evaluated over the spacetime hypersurface of the boundaries only, as specified by the support of the auxiliary fields. As the surfaces can be curved, this requires appropriate metric factors for the spatial integration measures (see below). The normalizing operator \mathcal{M}_∞ corresponds to the propagator at infinite separation of the surfaces and takes care of the self-energy subtraction. For the case of two surfaces, $\mathcal{M}_\infty^{-1} \mathcal{M}$ can be written as

$$\mathcal{M}_\infty^{-1} \mathcal{M} = \begin{pmatrix} 1 & \mathcal{M}_{11}^{-1} \mathcal{M}_{12} \\ \mathcal{M}_{22}^{-1} \mathcal{M}_{21} & 1 \end{pmatrix}, \quad (6)$$

where the matrix components distinguish between spacetime arguments "living" on the two different surfaces, i.e., $\alpha, \beta = 1, 2$. In the matrix product, an integration over the connecting intermediate spacetime points is implicitly understood. Due to the normalization with \mathcal{M}_∞ , only the off-diagonal elements are non-trivial, as they contain information about the propagation of fluctuations between the two different surfaces.

In order to compute the Casimir energy from Eq.(4) explicitly, we introduce the off-diagonal matrix $\Delta\mathcal{M}$,

$$\mathcal{M}_\infty^{-1} \mathcal{M} = \mathbf{1} + \begin{pmatrix} 0 & \mathcal{M}_{11}^{-1} \mathcal{M}_{12} \\ \mathcal{M}_{22}^{-1} \mathcal{M}_{21} & 0 \end{pmatrix} \equiv \mathbf{1} + \Delta\mathcal{M}, \quad (7)$$

¹Drawing the analogy to the electromagnetic case, the auxiliary fields can be thought of as charged sources which enforce the boundary conditions by means of their coupling to the fluctuating field [20].

such that a series expansion of the logarithm in Eq.(4) yields

$$E(H) = -\frac{\hbar c}{T_E} \frac{1}{2} \sum_{n=1}^{\infty} \frac{1}{2n} \text{Tr} (\Delta \mathcal{M}^{2n}). \quad (8)$$

Due to its off-diagonal structure, only even powers of $\Delta \mathcal{M}$ contribute to the Casimir energy. Performing the discrete trace over the matrix entries then yields by the cyclicity of the trace

$$E(H) = -\frac{\hbar c}{T_E} \frac{1}{2} \sum_{n=1}^{\infty} \frac{1}{n} \text{Tr} ((\mathcal{M}_{11}^{-1} \mathcal{M}_{12} \mathcal{M}_{22}^{-1} \mathcal{M}_{21})^n). \quad (9)$$

Thus, the Casimir energy can be understood as a sum over all generic "chains" of correlators between the surfaces. Starting from a generic point on surface S_1 , it is summed over all possible auxiliary-field or source correlators on the surface itself, followed by all possible ϕ propagations to the second surface S_2 , then generic source propagations on S_2 itself and all thinkable ways back to S_1 again. As a last step, these Casimir contributions are summed over all possible starting points. Within the language of scattering theory, $\mathcal{M}_{\alpha\alpha}^{-1}$ is related to the T matrix associated with scattering off the surface α [20].

Equation (9) is a useful starting point for explicit computations for a given configuration. For instance for two parallel Dirichlet planes, the trace turns out to be proportional to $1/(nH)^3$, yielding the scalar analogue to Casimir's celebrated result upon summation over n . The present formalism can straightforwardly be generalized to Neumann or electromagnetic boundary conditions by insertion of the corresponding δ functional constraint. The formalism has also been worked out for dielectric materials and fluctuations in media from which Lifshitz theory [36] can immediately be derived [28]. Arbitrarily curved surfaces require the knowledge of $\mathcal{M}_{\alpha\alpha}^{-1}$ for both surfaces, which is equivalent to working out the T matrix (or S matrix) of the corresponding scattering problem. Moreover, an efficient means to carry out the remaining summation and integrations is needed as well.

3 Scalar Casimir-Polder potential for a planar surface

The Casimir-Polder force between an atom and a plane wall at a distance H is easily derived from Lifshitz theory for two parallel plates. Consider one of the plates as consisting of a dilute dielectric with a dielectric permittivity $\epsilon = 1 + 4\pi\alpha N + \mathcal{O}(N^2)$. Here, α denotes the polarizability of the atoms in the surface and N is the number of atoms per unit area in the surface. Expanding the Casimir force from Lifshitz theory to first order in N yields the Casimir-Polder force between one of the atoms in the dielectric and the opposite wall as the prefactor at order N , see, e.g., [37]. This approach, however, cannot simply be applied to the case of an atom near a corrugated surface, since the prefactor at order N is an average over all possible atom positions at a given mean distance H above the corrugated surface. Hence, the important information about the dependence of the force on lateral coordinates is not available in this manner.

This information can be extracted following a different strategy. As the Casimir-Polder force arises from the atom's polarizability, i.e., the dipole transition induced by the fluctuating field, we can represent the atom by a compact surface with suitable polarization properties. The simplest case is, of course, a small sphere of radius r . In the limit $r \ll H$, the lowest non-vanishing inducible multipole moment, i.e., the dipole polarizability in this case, dominates the Casimir interaction between the small sphere and the corrugated surface. Hence, identifying this dipole polarizability of the sphere with that of an atom yields the Casimir-Polder law in this limit.

In this section, we proceed in exactly this fashion for the Dirichlet scalar case, i.e., we define the Casimir-Polder law in this case as the Casimir force between a small sphere of radius r and a corrugated wall at (mean) distance H in the limit of $r \ll H$. Here the lowest multipole contribution of a small sphere is that of a monopole excitation, hence the resulting power law [13, 15] with distance H will be different to that of the electromagnetic case, but it is straight forward to generalize this approach and computational strategy to the electromagnetic case.

As an exercise, we start with the planar case, identifying the planar surface with S_1 parametrized by the spatial coordinate $x_3 = 0$. The center of the sphere (surface S_2) of radius r is located at $x_1 = x_2 = 0$, $x_3 = H$. The singularity structure of the involved propagators is not entirely trivial and special care has to be taken to choose the proper order of limits and integrations. Of the four correlators occurring in Eq.(9), we begin with the contraction of the inverse propagator on the plane with the propagator between the surfaces.

Specifying Eq.(5) for the plane S_1 results in $\mathcal{M}_{11} = 1/[4\pi^2(\underline{x} - \underline{x}')^2]$, where $\underline{x} = (x_0, x_1, x_2) = (x_0, \vec{x}_{\parallel})$, i.e., the x_3 coordinate perpendicular to the plane drops out. By Fourier transforming the propagator to position space, we obtain the functional inverse,

$$\mathcal{M}_{11}^{-1} = 2\sqrt{-\underline{\nabla}^2}, \quad (10)$$

where $\underline{\nabla} = (\partial_0, \partial_1, \partial_2)$. This operator can immediately be contracted with the correlator between the plane and the sphere yielding

$$\int_{\underline{x}''} \mathcal{M}_{11}^{-1}(\underline{x}; \underline{x}'') \mathcal{M}_{12}(\underline{x}''; x') = \frac{1}{\pi^2} \frac{x'_3}{(x_3'^2 + (\underline{x} - \underline{x}')^2)^2} \equiv \Delta \mathcal{M}_{12}(\underline{x}; x'). \quad (11)$$

Since the setup is translationally invariant in time direction, it is expedient to Fourier transform the propagators to frequency space with respect to the time coordinate. The singularity structure can be well controlled using a proptime integral representation (with proptime S). In addition, we parametrize the surface of the sphere S_2 by spherical coordinates. The combined propagator then reads

$$\begin{aligned} \Delta \mathcal{M}_{12}(\zeta; \vec{x}_{\parallel}; \Omega) &= \frac{1}{\pi^{\frac{3}{2}}} (H + r \cos \theta) \int_0^{\infty} dS \sqrt{S} \exp\left(-\frac{\zeta^2}{4S}\right) \\ &\times \exp\left(-\left[(x_1 - r \cos \phi \sin \theta)^2 + (x_2 - r \sin \phi \sin \theta)^2 + (H + r \cos \theta)^2\right] S\right), \end{aligned} \quad (12)$$

where ζ denotes the imaginary frequency, the lateral coordinates on the plane are given by \vec{x}_{\parallel} , and Ω summarizes the azimuthal (θ) as well as the polar (ϕ) angle on the sphere.

Next, the inverse propagator \mathcal{M}_{22}^{-1} on the sphere S_2 can be determined from $\mathcal{M}_{22}^{-1}\mathcal{M}_{22} = \mathbb{1}$ which in terms of spherical coordinates reads

$$r^2 \int_{\Omega'} \mathcal{M}_{22}^{-1}(\zeta; \Omega; \Omega') \mathcal{M}_{22}(\zeta; \Omega'; \Omega'') = \frac{1}{r^2} \delta(\phi - \phi'') \delta(\cos \theta - \cos \theta''), \quad (13)$$

with \mathcal{M}_{22} given by Eq. (5), and $\int_{\Omega} = \int_0^{2\pi} d\phi \int_{-1}^1 d(\cos \theta)$. This equation can be solved for \mathcal{M}_{22}^{-1} by expanding all quantities in spherical harmonics $Y_{lm}(\Omega)$. As mentioned above, only the monopole order $l = 0 = m$ is relevant here, yielding

$$\mathcal{M}_{22}^{-1}(\zeta) \Big|_{\text{monopole}} = \frac{1}{4\pi r^2} \frac{|\zeta| \exp(r|\zeta|)}{\sinh(r|\zeta|)}. \quad (14)$$

The last propagator in the chain (Eq.(9)) evaluated on the surfaces S_1 and S_2 reads, again in proptime representation,

$$\mathcal{M}_{21}(\zeta; \Omega; \vec{x}_{\parallel}) = \int_0^{\infty} \frac{dT}{\sqrt{4\pi T}} e^{-\frac{\zeta^2}{16\pi^2 T}} e^{-4\pi^2 [(r \cos \phi \sin \theta - x_1)^2 + (r \sin \phi \sin \theta - x_2)^2 + (H + r \cos \theta)^2] T}. \quad (15)$$

With this, all correlators needed for the calculation of the Casimir energy between the sphere and the plane to monopole order are at hand. For the Casimir-Polder limit, it suffices to consider the lowest-order term of the n sum in Eq. (9), as discussed below. This term reads

$$\text{tr} (\Delta \mathcal{M}_{12} \mathcal{M}_{22}^{-1} \mathcal{M}_{21}) = \frac{T_E}{2\pi} \int_{\zeta} \int_{\vec{x}_{\parallel}} \int_{\Omega} \int_{\Omega'} r^4 \Delta \mathcal{M}_{12}(\zeta; \vec{x}_{\parallel}; \Omega) \mathcal{M}_{22}^{-1}(\zeta) \mathcal{M}_{21}(\zeta; \Omega'; \vec{x}_{\parallel}). \quad (16)$$

Let us now rescale all dimensionful quantities by the scale set by the sphere-plate distance H , i.e., $\vec{x}_{\parallel} \rightarrow \tilde{\vec{x}}_{\parallel} H$, $\zeta \rightarrow \frac{\tilde{\zeta}}{H}$, and consequently also the proptime parameters $S \rightarrow \frac{\tilde{S}}{H^2}$ and $T \rightarrow \frac{\tilde{T}}{H^2}$. In the limit $\frac{r}{H} \ll 1$, the inverse propagator on the sphere (14) can be expanded as

$$\mathcal{M}_{22}^{-1}(\tilde{\zeta}) = \frac{1}{4\pi} \frac{1}{r^3} \left(1 + \mathcal{O} \left(\frac{r}{H} |\tilde{\zeta}| \right) \right). \quad (17)$$

Even though ζ ranges from 0 to ∞ , the $\tilde{\zeta}$ integral receives its dominant contributions from $\tilde{\zeta} = \mathcal{O}(1)$, such that the order estimate of Eq. (17) is meaningful. The inverse propagator \mathcal{M}_{22}^{-1} thus becomes independent of the imaginary frequency to lowest order.

Collecting all the dimensionful factors from the rescaling, the trace Eq.(16) turns out to be of order $\mathcal{O} \left(\frac{r}{H^2} \right)$ and the remaining dimensionless integrals are a pure function of r/H . In the limit $r \ll H$, $\Delta \mathcal{M}_{12}(\tilde{\zeta}; \tilde{\vec{x}}_{\parallel}; \Omega)$ and $\mathcal{M}_{21}(\tilde{\zeta}; \Omega'; \tilde{\vec{x}}_{\parallel})$ become independent of Ω and Ω' , such that the two solid-angle integrations just contribute a factor of $16\pi^2$. We then obtain for Eq. (16):

$$\text{tr} (\Delta \mathcal{M}_{12} \mathcal{M}_{22}^{-1} \mathcal{M}_{21}) = T_E \frac{r}{H^2} 2 \int_{\tilde{\zeta}} \int_{\tilde{\vec{x}}_{\parallel}} \Delta \tilde{\mathcal{M}}_{12}(\tilde{\zeta}; \tilde{\vec{x}}_{\parallel}) \tilde{\mathcal{M}}_{21}(\tilde{\zeta}; \tilde{\vec{x}}_{\parallel}) + \mathcal{O} \left(\frac{r^2}{H^3} \right), \quad (18)$$

with the associated dimensionless propagators

$$\begin{aligned}\Delta\tilde{\mathcal{M}}_{12}(\tilde{\zeta}; \tilde{x}_{\parallel}) &= \frac{1}{\pi^{\frac{3}{2}}} \int_0^\infty d\tilde{S} \sqrt{\tilde{S}} e^{-(1+\tilde{x}_{\parallel}^2)\tilde{S}} \exp\left(-\frac{\tilde{\zeta}^2}{4\tilde{S}}\right) \\ \tilde{\mathcal{M}}_{21}(\tilde{\zeta}; \tilde{x}_{\parallel}) &= \frac{1}{2\sqrt{\pi}} \int_0^\infty \frac{d\tilde{T}}{\tilde{T}} e^{-4\pi^2(1+\tilde{x}_{\parallel}^2)\tilde{T}} \exp\left(\frac{\tilde{\zeta}^2}{16\pi^2\tilde{T}}\right).\end{aligned}\quad (19)$$

Finally, the remaining integrations in the trace expression can be performed straightforwardly in the following order: First, we perform the integral over $\tilde{\zeta}$ which is purely Gaussian, then the integral over \tilde{x}_{\parallel} is done using polar coordinates. At last, the integration over the variables of the proper time representation \tilde{T} and \tilde{S} is performed. The result for the lowest-order trace term then reads

$$\text{tr}(\Delta\mathcal{M}_{12}\mathcal{M}_{22}^{-1}\mathcal{M}_{21}) = T_E \frac{1}{4\pi} \frac{r}{H^2} + \mathcal{O}\left(\frac{r^2}{H^3}\right).\quad (20)$$

As higher orders in the n sum involve more propagators between the sphere and the plate and consequently further powers of H in the denominator, only the $n = 1$ term survives in the Casimir-Polder limit. Using Eq. (9), the energy between the sphere and the plane consequently yields in the Casimir-Polder limit $r \ll H$

$$E(H) = -\frac{\hbar c}{8\pi} \frac{r}{H^2} + \mathcal{O}\left(\frac{r^2}{H^3}\right),\quad (21)$$

which agrees with [13, 14, 15, 40, 41].

As we have seen, the spatial integrations over the surface of the sphere S_2 become trivial in the Casimir-Polder limit. Due to this fact, the integrations over the remaining lateral coordinates \tilde{x}_{\parallel} on the plate (cf. Eq. (18)) could also have been performed in momentum space since the flat plate itself is translationally invariant along these directions. However, in the following section we will extend our investigations to surfaces which are uniaxially structured along the direction x_1 . For this purpose, it is expedient to Fourier transform Eqs.(18) and (19) only with respect to the 2-component p_2 to momentum space. Due to a remaining Lorentz invariance in time and x_2 direction, the integrand only depends on the combination of momenta $\tilde{q} = \sqrt{\tilde{p}_2^2 + \tilde{\zeta}^2}$, such that we obtain

$$\text{tr}(\Delta\mathcal{M}_{12}\mathcal{M}_{22}^{-1}\mathcal{M}_{21}) = T_E \frac{2r}{H^2} \int_0^\infty d\tilde{q} \int_{-\infty}^\infty d\tilde{x}_1 \tilde{q} \Delta\tilde{\mathcal{M}}_{12}(\tilde{q}; \tilde{x}_1) \tilde{\mathcal{M}}_{21}(\tilde{q}; \tilde{x}_1) + \mathcal{O}\left(\frac{r^2}{H^3}\right).\quad (22)$$

After the execution of the \tilde{S} and \tilde{T} integrals, the propagators are given by modified Bessel functions of the second kind,

$$\begin{aligned}\Delta\tilde{\mathcal{M}}_{12}(\tilde{q}; \tilde{x}_1) &= \frac{1}{\pi} \frac{\tilde{q}}{\sqrt{1+\tilde{x}_1^2}} K_1\left(\tilde{q}\sqrt{1+\tilde{x}_1^2}\right), \\ \tilde{\mathcal{M}}_{21}(\tilde{q}; \tilde{x}_1) &= \frac{1}{2\pi} K_0\left(\tilde{q}\sqrt{1+\tilde{x}_1^2}\right).\end{aligned}\quad (23)$$

This representation is suitable for a generalization to a uniaxially corrugated surface, as is done in the next section.

4 Scalar Casimir-Polder potential for uniaxially corrugated surfaces

We now extend the above method to uniaxially arbitrarily corrugated surfaces S_1 . For simplicity, we consider deformations along x_1 which can be parametrized by a height function $h(x_1)$ (overhangs could also be included by an appropriate parametrization). The four-vector pointing onto the structured surface reads $x = (x_0, x_1, x_2, h(x_1))$. The center of the sphere is again located at $x_1 = x_2 = 0$, $x_3 = \bar{H}$. Here we write \bar{H} instead of just H to point out that it denotes the position of the sphere at a mean distance \bar{H} from the surface. For corrugated surfaces the actual distance H between the surface and the sphere is a function of the direction of corrugation $H = H(x_1)$ (cf. also Fig. 1). As for the planar situation considered earlier, it holds that $\bar{H} = H$.

As the inverse correlator on the sphere does not change and the correlators between the surfaces are still easy to compute, the main challenge for extending the previous calculations to corrugated surfaces is the determination of the inverse propagator \mathcal{M}_{11}^{-1} on the structured surface S_1 . For the planar case, translational invariance along the \underline{x} directions allows for diagonalization in momentum space and thus for an explicit solution as given in Eq.(10). By contrast, a structure on the surface breaks translational invariance in the direction of corrugation and the functional inverse of \mathcal{M}_{11} is not known analytically in the general case.

Let us first derive a suitable representation of the problem. The desired quantity \mathcal{M}_{11}^{-1} is defined by the equation

$$\int_{\vec{x} \in S_1} \mathcal{M}_{11}(\zeta; \vec{x}'; \vec{x}) \mathcal{M}_{11}^{-1}(\zeta; \vec{x}; \vec{x}'') = \delta(\vec{x}' - \vec{x}'') \Big|_{\vec{x}', \vec{x}'' \in S_1}. \quad (24)$$

where $\mathcal{M}_{11}(\zeta; \vec{x}'; \vec{x})$ is given by the Fourier transform of Eq. (5) with respect to the time coordinate. The integration over the surface in this case is defined by

$$\int_{\vec{x} \in S_1} = \int_{x_1} \int_{x_2} \sqrt{g(x_1)} \Big|_{x_3=h(x_1)}, \quad (25)$$

with the determinant of the induced metric given by $g(x_1) = 1 + (\partial_1 h(x_1))^2$. Thus Eq. (24) explicitly reads

$$\int_{\vec{x}_{\parallel}} \sqrt{g(x_1)} \mathcal{M}_{11}(\zeta; \vec{x}'_{\parallel}; \vec{x}_{\parallel}) \mathcal{M}_{11}^{-1}(\zeta; \vec{x}_{\parallel}; \vec{x}''_{\parallel}) = \frac{1}{\sqrt{g(x_1)}} \delta(\vec{x}'_{\parallel} - \vec{x}''_{\parallel}), \quad (26)$$

where \vec{x}_{\parallel} summarizes the flat coordinates x_1, x_2 along the two-dimensional surface.

In principle, we could try to solve this equation numerically and then plug in the solution into the our formulas for the Casimir energy. However, due to the singularity structure

of this equation, and also since we rather need the operator product $\Delta\mathcal{M}_{12} = \mathcal{M}_{11}^{-1}\mathcal{M}_{12}$ than \mathcal{M}_{11}^{-1} alone, we now multiply this equation with $\sqrt{g(x_1''')}\mathcal{M}_{12}(\zeta; \vec{x}_{\parallel}''; \vec{x}_{\parallel}''', x_3''')$ from the left and integrate both sides of Eq. (26) over the lateral coordinates \vec{x}_{\parallel}'' . One finds that

$$\int_{\vec{x}_{\parallel}} \sqrt{g(x_1)}\mathcal{M}_{11}(\zeta; \vec{x}_{\parallel}'; \vec{x}_{\parallel})\Delta\mathcal{M}_{12}(\zeta; \vec{x}_{\parallel}; \vec{x}_{\parallel}'', x_3''') = \mathcal{M}_{12}(\zeta; \vec{x}_{\parallel}'; \vec{x}_{\parallel}'', x_3'''), \quad (27)$$

where $\Delta\mathcal{M}_{12}$ explicitly includes the metric factor of the respective structure. Since the above matrix elements are still diagonal in p_2 in our uniaxial setup, we take the Fourier transform of Eq. (27) with respect to the 2-component. Slightly renaming the coordinates, we finally get

$$\int_{x_1} \sqrt{g(x_1)}\mathcal{M}_{11}(\zeta, p_2; x_1'; x_1)\Delta\mathcal{M}_{12}(\zeta, p_2; x_1; x_1'', x_3''') = \mathcal{M}_{12}(\zeta, p_2; x_1'; x_1'', x_3'''). \quad (28)$$

This equation is indeed more suitable for a numerical integration. As a final step, we again go over to dimensionless variables by rescaling all dimensionful quantities by the distance parameter H .² Also introducing the combined momentum $q = \sqrt{\zeta^2 + p_2^2}$ results in

$$\int_{\tilde{x}} \sqrt{g(\tilde{x})}\tilde{\mathcal{M}}_{11}(\tilde{q}; \tilde{x}'; \tilde{x})\Delta\tilde{\mathcal{M}}_{12}(\tilde{q}; \tilde{x}) = \tilde{\mathcal{M}}_{12}(\tilde{q}; \tilde{x}'), \quad (29)$$

where we have dropped the coordinate subscript “1”, since $x \equiv x_1$ is the only relevant direction in this Green’s function problem. The dimensionless propagators $\tilde{\mathcal{M}}_{12} \equiv \tilde{\mathcal{M}}_{21}$ and $\tilde{\mathcal{M}}_{11}$ are given by

$$\tilde{\mathcal{M}}_{11}(\tilde{q}; \tilde{x}'; \tilde{x}) = \frac{1}{2\pi}K_0\left(\tilde{q}\sqrt{(\tilde{x}' - \tilde{x})^2 + (\tilde{h}(\tilde{x}') - \tilde{h}(\tilde{x}))^2}\right), \quad (30)$$

$$\tilde{\mathcal{M}}_{12}(\tilde{q}; \tilde{x}') = \frac{1}{2\pi}K_0\left(\tilde{q}\sqrt{(\tilde{x}')^2 + (\tilde{h}(\tilde{x}') - 1)^2}\right), \quad (31)$$

where the metric factor reads

$$\sqrt{g(\tilde{x})} = \sqrt{1 + \left(\partial_{\tilde{x}}\tilde{h}(\tilde{x})\right)^2}, \quad \tilde{h}(\tilde{x}) = \frac{1}{H}h(\tilde{x}H). \quad (32)$$

Once Eq. (29) is solved for $\Delta\tilde{\mathcal{M}}_{12}$, the solution can be plugged into the Casimir energy formula. The scalar Casimir energy between a sphere and a surface which is uniaxially corrugated along x thus yields in the limit $r \ll H$

$$E = -\frac{\hbar c}{2} \frac{r}{H^2} \alpha + \mathcal{O}\left(\frac{r^2}{H^3}\right), \quad (33)$$

²Depending on the relevant geometric parameters, a rescaling with a different parameter such as a height amplitude or the wavelength of the corrugation may also be useful.

where

$$\alpha := 2 \int_0^\infty d\tilde{q} \int_{-\infty}^\infty d\tilde{x} \sqrt{g(\tilde{x})} \tilde{q} \Delta \tilde{\mathcal{M}}_{12}(\tilde{q}; \tilde{x}) \tilde{\mathcal{M}}_{21}(\tilde{q}; \tilde{x}), \quad (34)$$

is a dimensionless numerical factor that depends on the geometry parameters of the configuration (measured in units of H). The Casimir-Polder limit is obtained in the limit of the sphere radius r being much smaller than any other scale, $r \ll H, A, \lambda, \dots$, where A denotes a typical amplitude of the corrugation and λ a typical corrugation wavelength. The factor α thus is a function of $\alpha = \alpha(A/H, \lambda/H, \dots)$, but it is independent of r .

From a technical perspective, the result of Eqs. (33), (34) is very simple. It should be stressed that already the first trace term in the initial Casimir-energy formula (9) includes nine integrations for the trace: one over the imaginary frequency and four times two integrations over the lateral surface coordinates. Due to the trivial dependency of the integrand on the lateral coordinates of the sphere in the Casimir-Polder limit, the number of integrations was then reduced by four; moreover, the n sum is just replaced by its first term in this limit. The emerging translational invariance vertical to the direction of corrugation reduces the number of integrations by another two. Thus – instead of nine – we are left with three integrations: two of them are directly visible in Eq. (33), the third one is needed for the construction of $\Delta \mathcal{M}_{12}$ as a solution of Eq. (29). These simplifications make the Casimir-Polder limit accessible to numerical integration for arbitrary height profiles.

The resulting two integrals in Eq. (34) are both convergent, non-oscillatory and generically exhibiting a simple one-peak structure. The treatment of the singularity structure in the Green's functions equation (29), however, requires some care and is treated in the Appendix.

5 Sinusoidal corrugation

As a first nontrivial example, let us calculate the scalar Casimir-Polder potential for a sinusoidal corrugation, see Fig. 1. The potential for this structure is given by Eqs. (33), (34), where we use $h(x) = A \sin(\omega x + \phi)$ as a height function appearing in the propagators Eq. (31) as well as in the surface metric factor of Eq. (32). The phase ϕ is used to modulate the relative position of the structure beneath the sphere, since the latter is always fixed at $x = 0$. The mean distance between surface and atom is denoted by \bar{H} , whereas H characterizes the distance of the atom to the surface along the global surface normal. Hence H can be viewed as a function of ϕ in our conventions, $H = H(\phi)$ with $H(-\pi/2) = \bar{H} + A$ at the sine minimum and $H(\pi/2) = \bar{H} - A$ at the sine maximum, i.e., $H = 0$ always corresponds to atom-wall contact, where the limit $r \ll H$ is implicitly understood.

As the crucial building block for the Casimir-Polder potential, we solve the Green's function equation Eq. (29) numerically on a 1-D lattice in x direction. This requires to invert the propagator $\tilde{\mathcal{M}}_{11}$ on the corrugated surface. Even though the singularity of this propagator at coincident points is integrable in the continuum, the discretized version needs to deal with this singularity explicitly. This is done by introducing a regularization parametrized by a short-distance cutoff ϵ , which can be removed after the continuum limit

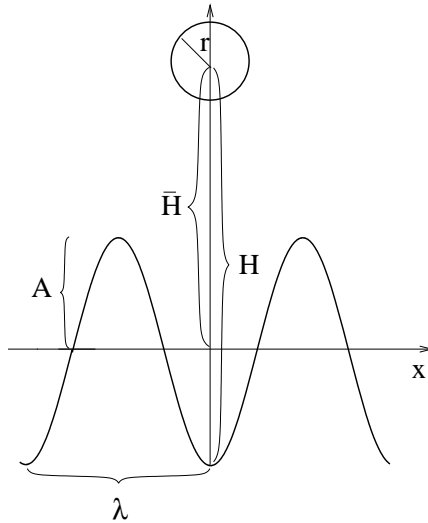


Figure 1: Sphere of radius r at a mean distance \bar{H} above a sinusoidally corrugated surface with amplitude A and wavelength $\omega = \frac{2\pi}{\lambda}$. In our conventions, we fix the sphere at the lateral coordinate $x = 0$, and effectively shift the structure function $h(x)$ by varying the phase ϕ . In this plot, we have set $\phi = -\pi/2$. The distance parameter H measures the sphere-surface distance along the global normal, such that $H = 0$ corresponds to sphere-surface contact for all values of ϕ .

has been taken. Details of how this procedure is implemented numerically are given in Appendix A.

In the following, we display our results for the Casimir-Polder energy always normalized with respect to the planar-surface case (for consistency, the normalization factor is also determined numerically). In this manner, the geometry-induced effects are better visible. Furthermore, we expect that these results for the scalar case give a qualitative estimate also for the electromagnetic case for which the normalizing prefactor has a different distance dependence.

In Fig. 2, we plot $E_{\text{sine}}/E_{\text{planar}}$ as a function of the horizontal position of the sphere above the sinusoidal corrugation between $\phi = -\pi$ and $\phi = \pi$ for three different mean separations $\bar{H}/A = 4, 2, 1.25$. The corrugation frequency is chosen to be $\omega A = 1$, all units are set by the corrugation amplitude A . As expected, above the corrugation minimum, e.g., at $x = -\pi/2$, the Casimir-Polder potential lies above the planar estimate since the plate bends towards the sphere. Analogously, above the corrugation maximum at $\pi/2$, $E_{\text{sine}}/E_{\text{planar}} < 1$. It is clear that the ratio $E_{\text{sine}}/E_{\text{planar}} \rightarrow 1$ as $\bar{H}/A \rightarrow \infty$, since the corrugation cannot be resolved anymore for greater distances. However, it is quite noticeable that the deviation from the planar case is still up to 10% even at large separations $\bar{H}/A = 4$.

In Fig. 3, we display $E_{\text{sine}}/E_{\text{planar}}$ as a function of the vertical position of the sphere above a minimum of the corrugation ($\phi = -\pi/2$) for different corrugation frequencies $\omega A = 1, 2, 3$. In the limits $H/A \rightarrow \infty$ and $H/A \rightarrow 0$, we find that $E_{\text{sine}}/E_{\text{planar}} \rightarrow 1$. This is expected, since in the first limit the corrugation of the plate cannot be resolved as it is too

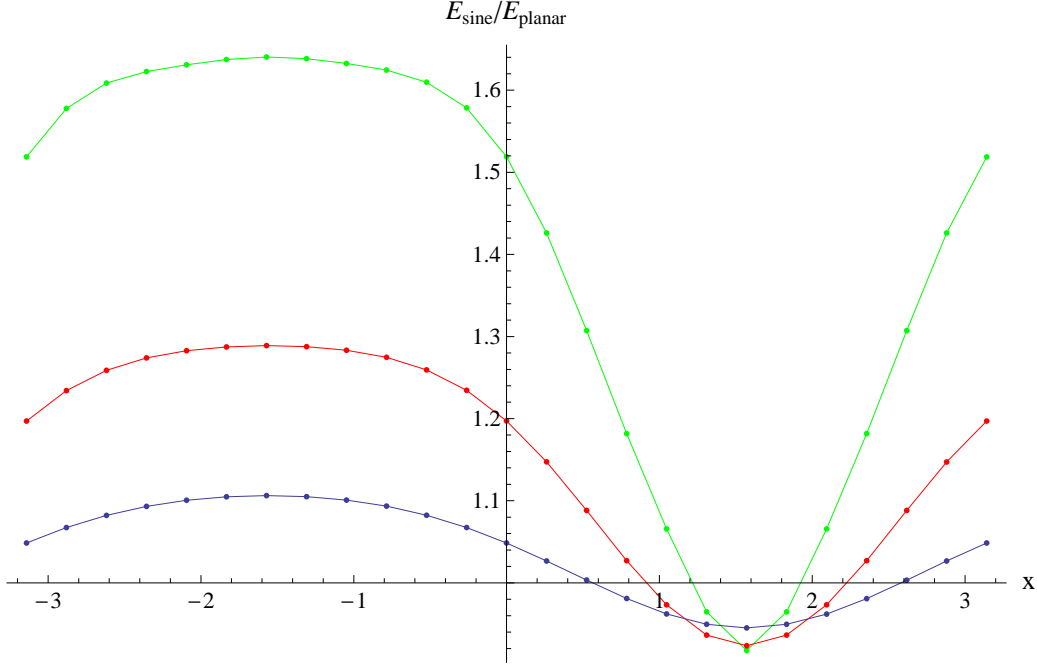


Figure 2: We give the ratio $E_{\text{sine}}/E_{\text{planar}}$ for three different separations $\bar{H}/A = 4$ (blue) $\bar{H}/A = 2$ (red) and $\bar{H}/A = 1.25$ (green), from bottom to top. The frequency of the sine structure is kept fixed at $\omega A = 1$. Above the corrugation trough at $\phi = -\frac{\pi}{2}$, it holds that $E_{\text{sine}}/E_{\text{planar}} > 1$, since the influence of the concavities of the corrugation towards the sphere is not accounted for by E_{planar} . Similarly, one finds $E_{\text{sine}}/E_{\text{planar}} < 1$ above the maximum of the corrugation at $\phi = \frac{\pi}{2}$. For larger ratios of \bar{H}/A , i.e. larger distances, the result approaches the planar case. Note that even at larger separations $\bar{H}/A = 4$, a pure planar approximation deviates from its true value by up to 10%.

small compared to the distance. In the second limit, the corrugation is irrelevantly large compared to the distance, i.e. the sphere does not notice it locally. In the region where $H \sim A$, the potential for the corrugated surface clearly deviates from the corresponding planar case. One can see that the effect becomes more pronounced for larger corrugation frequencies, i.e. shorter surface periodicity.

We identify various regimes which can be classified in terms of an anomalous dimension η which measures the deviation of the Casimir-Polder potential from the planar case,

$$E_{\text{corrugation}} \sim \frac{1}{H^{2+\eta}}, \quad (35)$$

with $\eta = 0$ for the planar case. At small distances, $H/A \ll 1$, we find a linear increase of the normalized potential $E_{\text{sine}}/E_{\text{planar}}$ with H/A , implying an anomalous dimension of $\eta = -1$. A linear fit to the short-distance data (not shown in Fig. 3) in the well yields $E_{\text{sine}}/E_{\text{planar}} \simeq 1 + \beta(H/A)$. The linear coefficient β depends on the frequency, $\beta = \beta(\omega/A) \simeq 0.5, 2.3, 5.2$ for $\omega A = 1, 2, 3$; within the numerical accuracy, this dependence is compatible with a power law $\beta \sim (\omega A)^2$.

At larger distances $H/A \sim \mathcal{O}(1)$, the normalized energy develops a peak. Various regimes can be identified near the peak and also in the drop-off region. The increase towards the peak as well as the decrease right beyond the peak can be characterized by power laws parametrized by an ω -dependent anomalous dimension. Towards the peak, we find $\eta \simeq -0.33, -0.57, -0.67$ for $\omega A = 1, 2, 3$, and the fit beyond the peak yields $\eta \simeq 0.4, 1.0, 1.6$ for $\omega A = 1, 2, 3$. For even larger distances near $H/A \simeq 10$, we observe that all normalized energies approach a universal curve being characterized by an anomalous dimension $\eta = 0.2$; in particular, the anomalous dimension shows no sizeable ω dependence anymore.

Whereas this observation might come as a surprise in the present formalism, it can easily be interpreted in the framework of the worldline picture of the quantum vacuum [12]. In this picture, quantum fluctuations are mapped onto random paths characterizing the spacetime trajectories of these fluctuations. In order to contribute to the Casimir interaction energy, such a trajectory has to intersect with both surfaces, the sphere and the corrugated plate in the present case. This implies that the fluctuation has an average extent of the order of the surface separation H . Due to isotropy of the vacuum fluctuations, the relevant worldlines also have a lateral extent of this order. This implies that the fluctuation integral also averages over structures of the corrugation which are smaller than H . Higher corrugation frequencies with $\omega H \gg 1$ thereby become irrelevant for the Casimir-Polder potential, as is demonstrated by the universal drop-off for larger H/A .

For even larger distances $H/A \gg 10$, the power law cannot continue for arbitrarily large H/A , since the Casimir-Polder potential eventually has to approach the planar limit. In this large-distance regime, we have only a few reliable numerical data points, as the discretization artifacts increase, once the lattice spacing approaches the corrugation wavelength. The available data is compatible with a logarithmic approach towards $E_{\text{sine}}/E_{\text{planar}} \rightarrow 1$ for $H/A \rightarrow \infty$.

Finally, we compute the Casimir-Polder potential above a maximum of the sine structure at $\phi = +\pi/2$. As expected, the Casimir-Polder energy is always smaller than in the planar case as the surfaces bends away from the atom and approaches the planar result in the two limits $H/A \rightarrow 0$ and $H/A \rightarrow \infty$, see Fig. 4. Starting from an initial decrease of the normalized energy for small distances H/A , a power-law decrease develops towards the dip with $\eta \simeq 0.09, 0.11, 0.11$ for $\omega A = 1, 2, 3$. Beyond the dip near $H/A \sim 1$, a power-law increase follows with anomalous dimension $\eta = -0.13, -0.16, -0.19$ for $\omega A = 1, 2, 3$, respectively. Again, we observe a linear ω dependence of η in this regime. Also, a second power-law regime is found for larger distances $H/A \gtrsim 10$ with an anomalous dimension $\eta = -0.07$ for the $\omega A = 1$ data. Due to an increase of the discretization artifacts, no reliable data for larger ω is available, such that the expected universality in this distance regime still needs to be shown.

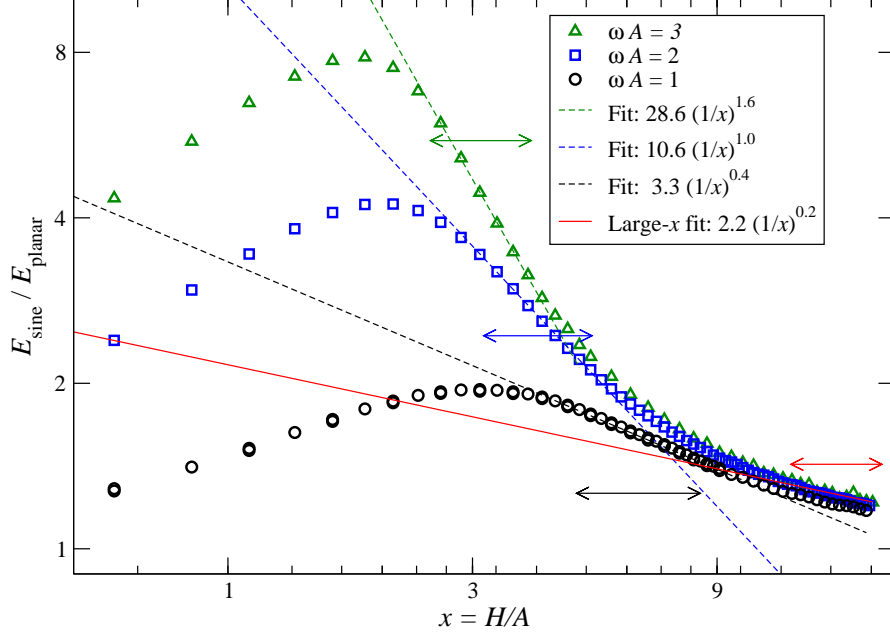


Figure 3: Normalized Casimir-Polder energy $E_{\text{sine}}/E_{\text{planar}}$ above a corrugation minimum $\phi = -\pi/2$ versus the normalized distance $x \equiv H/A$ for three different corrugation frequencies $\omega A = 1, 2, 3$, respectively. All units are set by the corrugation amplitude A . Small distances are governed by a linear increase with anomalous dimension $\eta = -1$, cf. Eq. (35). The drop-off beyond the peak is characterized by an ω -dependent anomalous dimension $\eta \simeq 0.4, 1.0, 1.6$ for $\omega A = 1, 2, 3$. At larger distances $H/A \sim 10$, all normalized energies approach a universal curve with $\eta \simeq 0.2$. The corresponding fit regions are indicated by horizontal arrows. Also the increase towards the peak can be parametrized by a power-law with anomalous dimensions $\eta \simeq -0.33, -0.57, -0.67$ for $\omega A = 1, 2, 3$ (not shown in the plot).

6 Sawtooth corrugation

As a second example, we study the Casimir-Polder potential for a sawtooth structure, where the wavelength λ is 2.8 in terms of the amplitude A , i.e. the dominant frequency of its Fourier decomposition is $\omega A \simeq 0.45$. These parameters reflect the specifications of a sawtooth structure used in a recent experiment [34]. For practical purposes, we actually use a smoothed, continuous sawtooth-like structure function with wavelength λ , starting at $h(0) = 0$, rising linearly to its maximum amplitude A at $h(0.8\lambda)$ and dropping linearly to zero again at $h(\lambda) = h(0)$.

In Fig. 5, we plot $E_{\text{sawtooth}}/E_{\text{planar}}$ above the corrugation minimum. Qualitatively, the result is similar to the sine structure and reveals the various analogous regimes. Quantitatively, the peak and consequently some of the anomalous dimensions are more pronounced. The increase towards the peak follows a power-law with anomalous dimension $\eta \simeq -0.3$. For the decrease right beyond the peak at $H/A \gtrsim 1$, we find an anomalous dimension

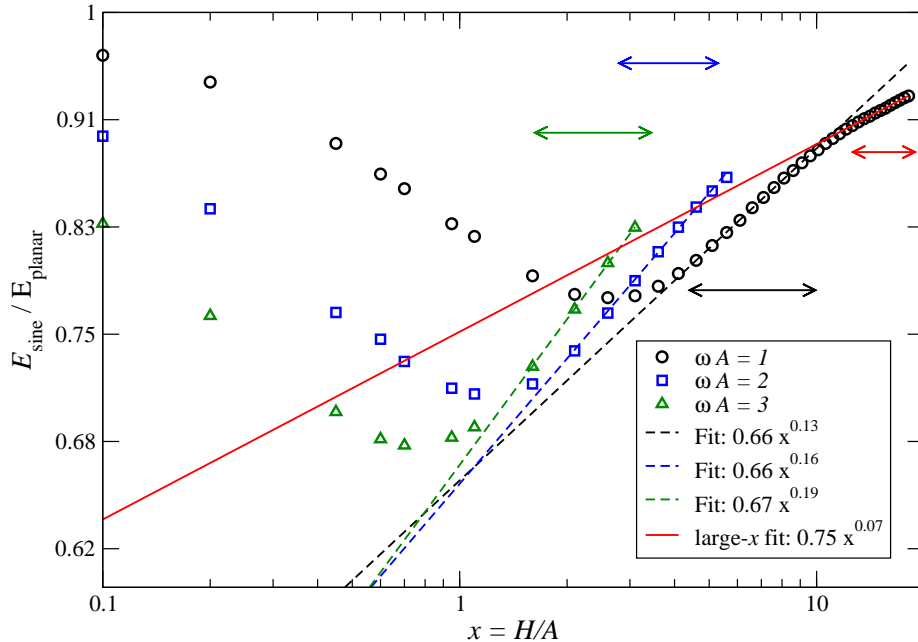


Figure 4: Normalized Casimir-Polder energy $E_{\text{sine}}/E_{\text{planar}}$ above a corrugation maximum $\phi = \pi/2$ versus the normalized distance $x \equiv H/A$ for three different corrugation frequencies $\omega A = 1, 2, 3$, respectively. All units are set by the corrugation amplitude A . The increase beyond the dip is characterized by an ω -dependent anomalous dimension $\eta \simeq -0.13, -0.16, -0.19$ for $\omega A = 1, 2, 3$. At larger distances $H/A \gtrsim 10$, a power law with $\eta \simeq -0.07$ is observed for the $\omega A = 1$ curve. The corresponding fit regions are indicated by horizontal arrows. Also the decrease towards the dip can be parametrized by a power-law with anomalous dimensions $\eta \simeq 0.09, 0.11, 0.11$ for $\omega A = 1, 2, 3$ (not shown in the plot).

of $\eta \simeq 1.1$. At larger distances $H/A \sim 10$, we again observe a second power law with anomalous dimension $\eta \simeq 0.2$ which agrees quantitatively with the anomalous dimension in the sinusoidal case.

Within the worldline picture of quantum fluctuations discussed above, this agreement can immediately be understood from the fact that the fluctuation integrals again average over the corrugation structures small compared to the distance parameter H .

7 Conclusions

In this work, we have presented a new approach to Casimir-Polder forces for corrugated surfaces which does not rely on a perturbative ordering of length scales. Our approach is based on the constrained-functional-integral approach [26] which – for uniaxial corrugations – boils down to a one-dimensional Green’s function equation along the corrugation direction. This equation is accessible to direct numerical integration provided the integrable singularity structures are carefully taken into account. For simplicity, we have studied the

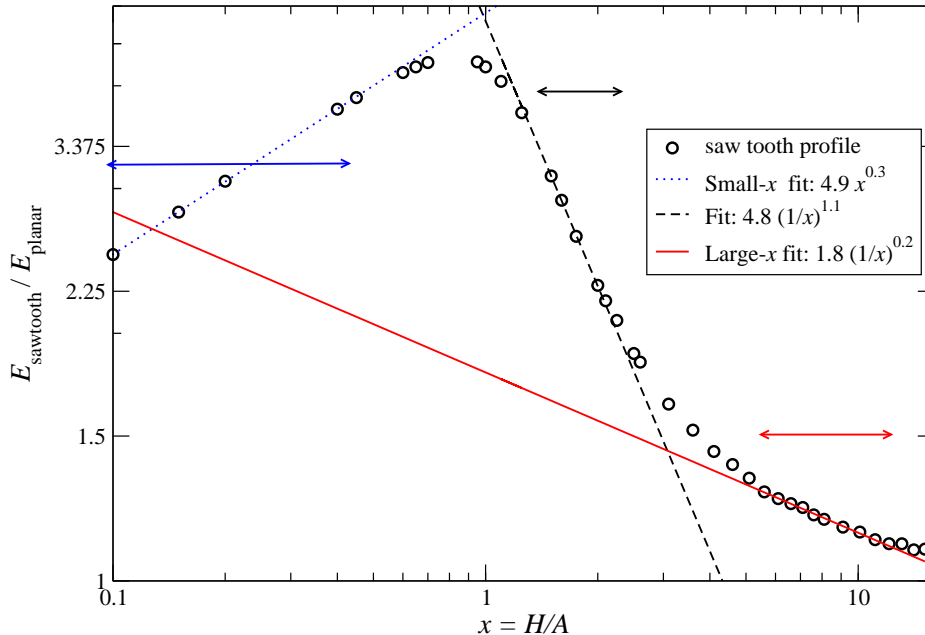


Figure 5: Normalized Casimir-Polder energy $E_{\text{sawtooth}}/E_{\text{planar}}$ above a corrugation minimum of the saw-tooth profile (see text) versus the normalized distance $x \equiv H/A$ for $\omega A \simeq 0.45$. All units are set by the corrugation amplitude A . The increase towards the peak is governed by a power-law with anomalous dimension $\eta = -0.3$. The drop-off beyond the peak is characterized by an ω -dependent anomalous dimension $\eta \simeq 1.1$. At larger distances $H/A \sim 10$, the normalized energy approaches a curve similar to the curves for the sine structure with $\eta \simeq 0.2$. The corresponding fit regions are indicated by horizontal arrows.

Dirichlet scalar analogue of the electromagnetic Casimir-Polder case, defined by a fluctuating scalar field satisfying Dirichlet boundary conditions on the surface and the “atom”; the latter is modeled by a small sphere in the limit of zero radius in our approach.

Two periodic corrugations, a sine and a sawtooth function, are studied in detail, revealing various regimes with distinct distance dependencies. For a classification of these distance dependencies, we have introduced the notion of an anomalous dimension characterizing the deviation of the distance power law of the Casimir-Polder potential from the planar case. In particular, the larger-distance behavior $H/A \gtrsim 1$ exhibits two different power-law behaviors with positive anomalous dimensions above a corrugation minimum and with negative anomalous dimensions above a corrugation maximum. In either case, the intermediate distance behavior near $H/A \sim 1$ is characterized by an anomalous dimension, the modulus of which increases linearly with the corrugation frequency.

Most importantly, we have identified a larger-distance regime near $H/A \sim 10$ where all data above a corrugation minimum is characterized by a universal anomalous dimension $\eta \simeq 0.2$. This anomalous dimension still depends on the position above the corrugation, e.g., $\eta \simeq 0.07$ above a minimum, but we have found no dependence neither on the shape

of the periodic profile nor on the frequency as long as $\omega H \gg 1$. Within the worldline picture of the quantum vacuum where fluctuation averages are mapped onto random-path averages, this universality can be understood from the fact that small-scale structures are averaged out and become irrelevant at larger distances. This observation also justifies to use the notion of universality and anomalous dimensions, since the fluctuation averages are reminiscent to those of critical phenomena. The resulting Casimir-Polder potential can be viewed as a “renormalized” effective Hamiltonian where the running IR cutoff is provided by the atom-wall distance.

We would like to stress that this universality as well as the nontrivial power-law behavior cannot be deduced from a perturbative analysis, since perturbation theory in the height profile is a Taylor expansion in powers of A/H , whereas a nontrivial anomalous dimension $\eta \in \mathbb{R}$ corresponds to a $(A/H)^\eta$ dependence of the Casimir-Polder law. Therefore, the development and use of a nonperturbative method was absolutely crucial for this work.

Even though we only considered the Dirichlet scalar case, the constrained-functional-integral formalism can straightforwardly be extended to the electromagnetic case as well [28] which carries over to a straightforward generalization of our techniques. Since no monopole fluctuations exist in the electromagnetic case due to charge conservation, the leading-order Casimir-Polder potential in the planar case follows a $\sim 1/H^4$ distance law instead of $\sim 1/H^2$ in the present case. But apart from this, we do not expect further dramatic differences as far as the corrugation-dependencies are concerned. Therefore, the Dirichlet scalar case may be taken as a rough qualitative estimate also for the electromagnetic case; in particular, we expect the occurrence of anomalous dimensions of the same order of magnitude.

The notion of anomalous dimension is also of direct use for Casimir-Polder experiments based on quantum reflection such as the atom-beam spin echo technique [32, 33, 5]. In a certain sense, such an experiment measures the local shape of a potential and thus is directly sensitive to anomalous dimensions. Indeed, the results of recent measurements with corrugated surfaces can be parametrized by anomalous dimensions of order one. Of course, a direct comparison between our results and those of an experiment requires much more than the computation of anomalous dimensions, since the atoms near the wall can move into all directions and not only along the global normal. The full Casimir-Polder potential needs to be mapped out, and the time-dependent quantum reflection problem in this potential has to be solved. In any case, the approach presented here lays the foundation for this future program.

Acknowledgments

The authors gratefully acknowledge useful discussions with T. Emig and R.L. Jaffe. HG thanks the DFG for support under grant No. GI 328/5-1 (Heisenberg program).

A Numerical procedure

In the following, we detail our implementation for the numerical evaluation of the Casimir-Polder potential for arbitrary uniaxial corrugations, cf. sections 5 and 6. We proceed as follows: First, we solve the Green's function equation for the associated propagator $\Delta\mathcal{M}_{12}$ Eq.(29) by discretizing the equation with respect to the spatially lateral coordinate x . The result is then plugged into Eq. (33), yielding the Casimir-Polder energy upon integration of \tilde{x} and \tilde{q} .

For the first step, we introduce two parameters: $\pm L_x$ which labels the left and right cutoff of the spatial integration, and N_x denoting the number of spatial discretization sites, respectively. In the end, we remove the discretization by a continuum extrapolation $N_x \rightarrow \infty$.

In principle, L_x is a physical parameter encoding the physical size of the surface. Here, we will not make use of this option of studying finite-size effects, but compute the Casimir-Polder potential in the ideal infinite surface limit by extrapolating to $L_x \rightarrow \infty$. For this, we fix the position of the sphere above the plate at $x = 0$ and choose a symmetric cutoff for $x \in [-L_x, L_x]$. The two limits, continuum ($N_x \rightarrow \infty$) and infinite-length ($L_x \rightarrow \infty$) limit, have to be taken such that the lattice spacing $a_x = 2L_x/N_x$ also goes to zero, $a_x \rightarrow 0$. This can be ensured by choosing a suitable function $L_x = L_x(N_x)$, satisfying $L_x(N_x \rightarrow \infty) \rightarrow \infty$ and $L_x(N_x)/N_x \rightarrow 0$ as $N_x \rightarrow \infty$. In practice, we use

$$L_x(N_x) = \frac{a_{0x}}{2} \sqrt{N_x N_{0x}}, \quad (36)$$

where a_{0x} defines a reference lattice spacing at a reference site number $N_x = N_{0x}$. Note that the lattice spacing $a_x \equiv a_x(N_x) = 2L_x(N_x)/N_x = a_{0x} \sqrt{N_{0x}/N_x}$ goes to zero in the continuum limit $N_x \rightarrow \infty$, while $L_x \rightarrow \infty$ approaches the infinite length limit. Therefore all these idealized limits are controlled by one parameter: N_x . In practice, the finite-length corrections have always been found to be small compared to discretization effects. In general, it suffices to choose the reference lattice spacing such that typically $L_x(N_{0x}) = 2H$, where N_{0x} specifies the coarsest lattice in the calculation.

One serious complication arises when discretizing Eq.(29): due to the pole of the zeroth Bessel function K_0 at its origin, the matrix \mathcal{M}_{11}^{ij} that emerges upon the discretization of the spatial arguments diverges in its diagonal entries, i.e., for the case when the spatial discretization sites lie on top of each other. Whereas these divergencies are integrable when solving the problem in the continuum, the discretized matrix becomes singular. Therefore, a regularization procedure is required that facilitates to first take the continuum limit before the regulator can safely be removed. Here, we use a UV regularization for the propagator in Eq. (30) for small arguments z controlled by a small parameter ϵ :

$$\mathcal{M}_{11}(z) = \begin{cases} \frac{1}{2\pi} K_0(z) & , z \leq \epsilon \\ -\frac{1}{2\pi} (\ln(z + \epsilon) - K_0(\epsilon) - \ln(2\epsilon)) & , z > \epsilon \end{cases}, \quad (37)$$

where z summarizes all arguments of the propagator including both spatial and momentum contributions, entering the Bessel function as a single argument, cf. Eq. (30). The physical

result is expected to arise in the limits $N_x \rightarrow \infty$ and $\epsilon \rightarrow 0$ with the continuum limit to be taken first before the regulator is removed.

In a numerical calculation where N_x and ϵ are always finite, the order of limits done by extrapolation requires a careful choice of N_x and ϵ . It is already intuitively clear that smaller values of ϵ require larger values of N_x , since the proper resolution of a more pronounced singularity for smaller ϵ needs a finer lattice. As the pole in the inverse propagator on the corrugated surface S_1 persists irrespectively of the corrugation, the numerical discretization and regularization errors can be tested in the planar situation where the analytical result is known (cf. section 3): there, the dimensionless factor α amounts to $\frac{1}{4\pi}$.

In Fig. 6, we plot α as a function of the inverse number of discretization sites $1/N_x$ for different values of the cutoff ϵ in the planar case. The values for α depend linearly on $1/N_x$ to a good approximation and appear to converge for different cutoffs ϵ as $1/N_x \rightarrow 0$.

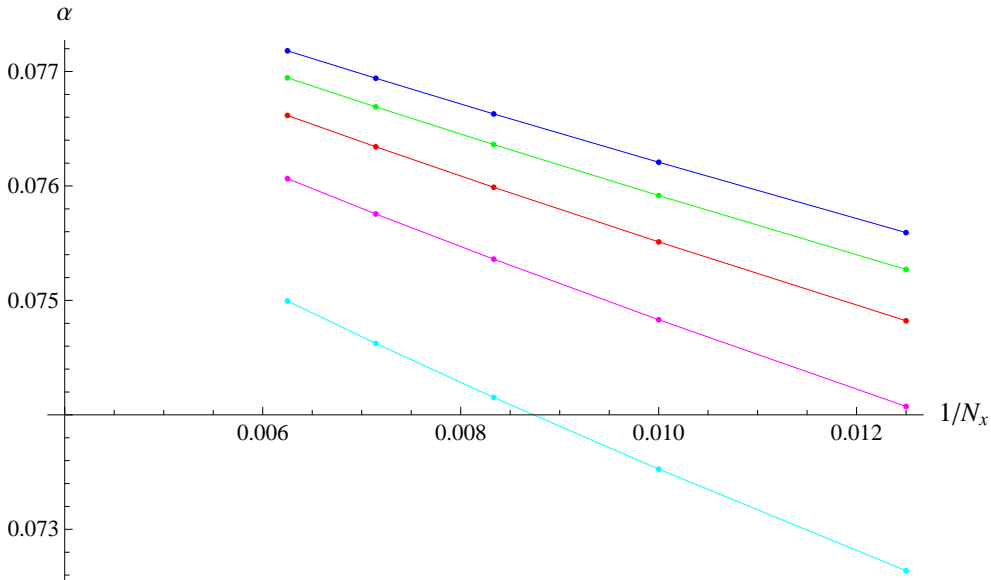


Figure 6: Numerical values for the dimensionless contribution of the lowest-order trace term α (34) in the plane-sphere configuration as a function of the inverse number of discretization sites N_x for five values of the cutoff parameter ϵ , $\epsilon = 5 \cdot 10^{-5}, 2 \cdot 10^{-4}, 4 \cdot 10^{-4}, 6 \cdot 10^{-4}, 8 \cdot 10^{-4}$ from bottom to top. The analytical value for α is $1/(4\pi) \approx 0.07958$. For fixed ϵ , the result scales linearly with the discretization $1/N_x$ to a good approximation and appears to converge with $1/N_x \rightarrow 0$, but it is also visible that the gradients of the curves grow as $\epsilon \rightarrow 0$.

Next, we extrapolate the values for α linearly to $1/N_x = 0$; as the linearity persists to a good approximation for all values of N_x in Fig. 6, it suffices to use only two data points for the extrapolation. We give two separate extrapolations for $N_x = 80, N_x = 100$ and $N_x = 180, N_x = 200$, respectively. The result is plotted as a function of ϵ in Fig. 7. Recall that the analytical value for α yields $1/(4\pi) \approx 0.07958$ for the flat plate, which is chosen

to be exactly the origin of the coordinate system in Fig. 7.

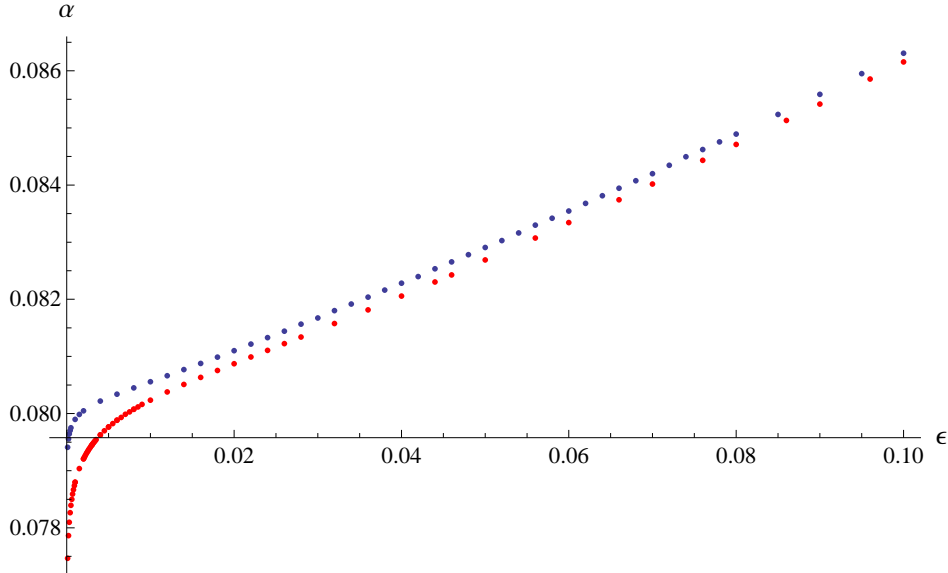


Figure 7: Continuum limit for α as defined in Eq. (34) after linear extrapolation to $1/N_x \rightarrow 0$ (using $1/N_x = 80$ and $1/N_x = 100$ in the lower (red) and $1/N_x = 180$ and $1/N_x = 200$ data in the upper (blue) curve) as a function of the cutoff parameter ϵ for values of $10^{-4} < \epsilon < 0.1$. The intersection between the two plot axes is chosen at $\alpha = \frac{1}{4\pi}$, which is the exact value for α in the planar case. The two curves can both be separated into several regimes. Consider e.g. the lower curve: It holds that for very small values of ϵ ($\epsilon \lesssim 0.0045$), the result for α lies below the analytical value and appears to diverge as $\epsilon \rightarrow 0$, since the integrable singularity is not resolved by the number of sites N_x used for the extrapolation. In the region $0.01 \lesssim \epsilon \lesssim 0.04$, $\alpha(\epsilon)$ grows linearly with ϵ (for $\epsilon \gtrsim 0.04$, we identify a $\alpha(\epsilon) \sim \epsilon^2$ dependence). An extrapolation $\alpha(\epsilon \rightarrow 0)$ in the range $0.01 \lesssim \epsilon \lesssim 0.04$ thus provides an estimate for the cutoff-independent value of α (cf. Eq. (38)). For the upper, blue curve the respective regimes can also be identified. However, since the resolution of the structure is increased by a greater number of N_x , the important linear regime is shifted to lower ϵ -values.

The graphs in Fig. 7 can in fact be divided into several regions. Consider, e.g. the lower curve: For values of $\epsilon \lesssim 0.0045$, the extrapolation $1/N_x \rightarrow 0$ underestimates α and even appears to diverge as $\epsilon \rightarrow 0$. This agrees with our expectation that the integrable singularity in the Green's function equation has not been properly resolved with the underlying discretization; higher values of N_x would be required for a more reliable estimate. This small- ϵ branch therefore corresponds to a region in parameter space where the result arising from the correct order of limits (first $N_x \rightarrow \infty$, then $\epsilon \rightarrow 0$) is not yet visible.

At about $\epsilon \gtrsim 0.01$, α exhibits a clear linear growth with ϵ . For $\epsilon \gtrsim 0.04$, higher power corrections become visible. We conclude that the cutoff-dependent factor $\alpha(\epsilon)$ can well be

approximated by a power series above the value of $\epsilon \gtrsim 0.01$,

$$\alpha(\epsilon) = \alpha_0 + \alpha_1\epsilon + \alpha_2\epsilon^2 + \dots \quad (38)$$

Thus, by extrapolating the values for α to $\epsilon = 0$ in the region where α grows linearly with ϵ , we obtain a cutoff-independent result α_0 . As for the extrapolation $1/N_x \rightarrow 0$, it suffices to use only two sites in ϵ in the linear regime to extract α_0 ; of course, also more data points for a higher polynomial fit could easily be employed at the expense of computing time.

From Fig. 7, we identify for the $1/N_x = 80$ and $1/N_x = 100$ data $0.01 \lesssim \epsilon \lesssim 0.04$ as the region where $\alpha(\epsilon)$ grows linearly with ϵ with only very small higher-power corrections. Choosing the data points at $\epsilon = 0.02$ and $\epsilon = 0.025$ for a linear extrapolation, we obtain $\alpha_0 = 0.07970$ which nicely matches the analytical value, the error being below 1%.³ As a check of the continuum limit, an extrapolation using $N_x = 180$ and $N_x = 200$ sites (upper curve in Fig. 7, again at $\epsilon = 0.02$ and $\epsilon = 0.025$) yields $\alpha_0 = 0.0799554$, which is also within 1% of the analytical value. The small deviations between these two results can be taken as a measure for the overall numerical uncertainty. One can see, that choosing larger values of N_x for the continuum extrapolation also results in an extension of the linear ϵ regime to smaller ϵ values.

It should be mentioned that the choice of required N_x values also depends on the corrugation parameters. For instance for high values of the corrugation frequency, a better resolution is needed; as a rule of thumb, the lattice spacing a_x should always be smaller than the smallest dominant wave length of the corrugation.

All numerical calculations for this work have been performed on a standard desktop computer with standard linear algebra packages. Depending on the discretization, the calculation of a typical data point including continuum limit and regulator removal takes on the order of seconds to several minutes. Since the linear-algebra routines scale with $\sim N_x^3$, the computational cost for very fine discretizations can rapidly increase.

References

- [1] H.B.G. Casimir, Kon. Ned. Akad. Wetensch. Proc. **51**, 793 (1948).
- [2] H.B.G. Casimir and D. Polder, Phys. Rev. **73**, 360 (1948).
- [3] S. K. Lamoreaux, Phys. Rev. Lett. **78**, 5 (1997).
- [4] U. Mohideen and A. Roy, Phys. Rev. Lett. **81**, 4549 (1998);
 A. Roy, C. Y. Lin and U. Mohideen, Phys. Rev. D **60**, 111101 (1999);
 T. Ederth, Phys. Rev. A **62**, 062104 (2000);

³For the study of corrugated surfaces, we have carefully studied whether the interval linear in ϵ is shifted and the extrapolation has to be adjusted accordingly. It turns out that the endpoints of the linear region are indeed slightly shifted for structured surfaces, but the sampling points $\epsilon = 0.02$ and $\epsilon = 0.025$ have always been in the linear region for all examples.

- H.B. Chan, V.A. Aksyuk, R.N. Kleiman, D.J. Bishop and F. Capasso, *Science* **291**, 1941 (2001);
- F. Chen, U. Mohideen, G.L. Klimchitskaya and V.M. Mostepanenko, *Phys. Rev. Lett.* **88**, 101801 (2002);
- G. Bressi, G. Carugno, R. Onofrio and G. Ruoso, *Phys. Rev. Lett.* **88**, 041804 (2002) [arXiv:quant-ph/0203002].
- [5] V. Druzhinina and M. DeKieviet, *Phys. Rev. Lett.* **91**, 193202 (2003).
- [6] R. S. Decca, D. Lopez, E. Fischbach, G. L. Klimchitskaya, D. E. Krause and V. M. Mostepanenko, *Phys. Rev. D* **75**, 077101 (2007) [arXiv:hep-ph/0703290].
- [7] B.V. Derjaguin, I.I. Abrikosova, E.M. Lifshitz, *Q.Rev.* **10**, 295 (1956); J. Blocki, J. Randrup, W.J. Swiatecki, C.F. Tsang, *Ann. Phys. (N.Y.)* **105**, 427 (1977).
- [8] G. Feinberg and J. Sucher, *Phys. Rev. A* **2**, 2395 (1970).
- [9] R. Balian and B. Duplantier, *Annals Phys.* **112**, 165 (1978).
- [10] M. Schaden and L. Spruch, *Phys. Rev. A* **58**, 935 (1998); *Phys. Rev. Lett.* **84** 459 (2000).
- [11] A. Scardicchio and R. L. Jaffe, *Nucl. Phys. B* **704**, 552 (2005); *Phys. Rev. Lett.* **92**, 070402 (2004).
- [12] H. Gies, K. Langfeld and L. Moyaerts, *JHEP* **0306**, 018 (2003) [arXiv:hep-th/0311168].
- [13] H. Gies and K. Klingmuller, *J. Phys. A* **39** 6415 (2006) [arXiv:hep-th/0511092].
- [14] H. Gies and K. Klingmuller, *Phys. Rev. Lett.* **96**, 220401 (2006) [arXiv:quant-ph/0601094]; *Phys. Rev. D* **74**, 045002 (2006) [arXiv:quant-ph/0605141].
- [15] A. Bulgac, P. Magierski and A. Wirzba, *Phys. Rev. D* **73**, 025007 (2006) [arXiv:hep-th/0511056]; A. Wirzba, A. Bulgac and P. Magierski, *J. Phys. A* **39** (2006) 6815 [arXiv:quant-ph/0511057].
- [16] O. Kenneth and I. Klich, *Phys. Rev. Lett.* **97**, 160401 (2006); [arXiv:quant-ph/0707.4017].
- [17] T. Emig, R. L. Jaffe, M. Kardar and A. Scardicchio, *Phys. Rev. Lett.* **96** (2006) 080403.
- [18] M. Bordag, *Phys. Rev. D* **73**, 125018 (2006); *Phys. Rev. D* **75**, 065003 (2007).
- [19] R. B. Rodrigues, P. A. Maia Neto, A. Lambrecht and S. Reynaud, *Phys. Rev. Lett.* **96**, 100402 (2006) [arXiv:quant-ph/0603120]; *Phys. Rev. A* **75**, 062108 (2007).

- [20] T. Emig, N. Graham, R. L. Jaffe and M. Kardar, [arXiv:cond-mat/0707.1862]; [arXiv:cond-mat/0710.3084].
- [21] K. A. Milton and J. Wagner, Phys. Rev. D **77**, 045005 (2008) [arXiv:0711.0774 [hep-th]]; J. Phys. A **41**, 155402 (2008) [arXiv:0712.3811 [hep-th]].
- [22] K. A. Milton, P. Parashar and J. Wagner, arXiv:0806.2880 [hep-th].
- [23] K. A. Milton, arXiv:0809.2564 [hep-th].
- [24] F. D. Mazzitelli, D. A. R. Dalvit and F. C. Lombardo, New J. Phys. **8**, 240 (2006); D. A. R. Dalvit, F. C. Lombardo, F. D. Mazzitelli and R. Onofrio, Phys. Rev. A **74**, 020101 (2006).
- [25] A. Rodriguez, M. Ibanescu, D. Iannuzzi, F. Capasso, J.D. Joannopoulos, and S.G. Johnson, Phys. Rev. Lett. **99**, 080401 (2007).
- [26] M. Bordag, D. Robaschik and E. Wieczorek, Annals Phys. **165**, 192 (1985).
- [27] T. Emig, A. Hanke and M. Kardar, Phys. Rev. Lett. **87** (2001) 260402.
- [28] T. Emig and R. Buscher, Nucl. Phys. B **696**, 468 (2004).
- [29] I. Cervero-Pelaez, K. A. Milton, P. Parashar and K. V. Shajesh, arXiv:0805.2776 [hep-th]. arXiv:0805.2777 [hep-th].
- [30] V.B. Bezerra, G.L. Klimchitskaya, and C. Romero, Phys. Rev. A **61**, 022115 (2000).
- [31] D.A.R. Dalvit, P.A. Maia Neto, A. Lambrecht, and S. Reynaud, Phys. Rev. Lett. **100**, 040405 (2008).
- [32] M. DeKieviet, D. Dubbers, C. Schmidt, D. Scholz and U. Spinola, Phys. Rev. Lett. **75**, 1919 (1995)
- [33] M. DeKieviet, D. Dubbers, M. Klein, C. Schmidt and M. Skrzypczyk, Surf. Sci. **377-379**, 1112 (1997)
- [34] U. Warring, V. Druzhinina, L. Arntzen, T. Stöferle and M. DeKieviet, in preparation (2008).
- [35] D.C. Roberts and Y. Pomeau, Phys. Rev. Lett. **95**, 145303 (2005) [arXiv:cond-mat/0503706].
- [36] E. M. Lifshitz, Sov. Phys. JETP **2**, 73 (1956).
- [37] J.F. Babb, G.L. Klimchitskaya, and V.M. Mostepanenko, Phys. Rev. A **70**, 042901 (2004).
- [38] M. Bordag, D. Robaschik and Wieczorek, E. 1985, Annals of Physics, 165, 192

- [39] T. Emig, A. Hanke, R. Golestanian and M. Kardar, PhysRevA.67.022114, [arXiv:cond-mat/0211193]
- [40] T.Emig, [arXiv:cond-mat/0712.2199v1]
- [41] P.A. Maia Neto, A. Lambrecht, and S. Reynaud, Phys. Rev. A **78**, 012115 (2008).